Lasers in Manufacturing and Materials Processing
https://doi.org/10.1007/s40516-026-00331-1

RESEARCH

Core-ring Laser Welding: the Influence of Ring Diameter on the Capillary Dynamics and the Formation of Pores in the Resulting Weld

Felix Zaiß[1] · John Powell[1] · Michael Haas[1,6] · Christian Diegel[2] · Klaus Schricker[2,7] · Jean Pierre Bergmann[2] · Christoph Spurk[3] · Marc Hummel[3,4] · Alexander Olowinsky[4] · Felix Beckmann[5] · Julian Moosmann[5] · Christian Hagenlocher[1] · Thomas Graf[1]

Received: 28 November 2025 / Revised: 16 January 2026 / Accepted: 30 January 2026
© The Author(s) 2026

Abstract

Double-core fibers that deliver laser beams with adjustable amounts of power to the central core and the surrounding ring component of the fiber are of major interest for optimizing laser welding processes. However, the central focussed laser spot and the ring diameters are fixed by the fiber dimensions, the focusing optics, and the laser systems involved. This work investigates the influence of different ring beam diameters, with a constant central spot diameter, on the capillary dynamics and the formation of pores in the resulting welds in 1.4301 stainless steel (X5CrNi18-10, AISI 304). The different core-ring configurations were achieved using specially designed beam-shaping optics. The generation of pores during the welding process was examined by means of synchrotron X-ray imaging. The results show that different ring diameters have a profound effect on the melt pool geometry, the capillary shape and the location of the capillary collapse which gives rise to pore formation in the weld. In the examples presented here, larger ring diameters extended the melt pool in the direction of welding without contributing directly to the capillary evaporation. In this case the narrow, deep capillaries which are created by the core beam alone can bulge and collapse, trapping vapor and gas to create large pores. If, however, the ring beam has a small enough diameter, it can help to produce a wider capillary which does not trap gas and create pores in the same way. The mechanisms by which large bubbles in the melt can result in non-spherical pores in the weld are also explained.

Keywords Core-ring laser welding · Pore formation · Synchrotron x-ray imaging · Stainless steel · Capillary dynamics · Multicore fiber system · Non-spherical pore formation.

Extended author information available on the last page of the article

Published online: 11 March 2026

Introduction

In laser welding, a high-power laser beam is focussed on the surface of the workpiece and moved in relation to it. This results in heating, melting and, in the case of deep penetration welding, local vaporization of the material to form a vapor-filled cavity, referred to as a capillary [1–4].

Figure 1 shows a simplified sketch of the deep penetration laser welding process, with a laser beam moving in the positive x-direction and creating a capillary. The length of the capillary opening at the surface (z = 0), in the direction of travel, is referred to longitudinal capillary aperture d_x and the distance from the surface to the tip of the capillary is referred to as capillary depth s_{cap}. The capillary cross section in the y-z plane at x = 0 can be seen on the right-hand side of the image. Melt generated in front of the capillary flows around it through a melt channel and into the melt pool behind. The distance between the melt-solid interface and the edge of the capillary at x = 0 and z = 0 is referred to as channel width w_{melt}. A change of this melt channel width is linked to a change in the melt channel cross-section which affects the melt flow velocity around the capillary [5]. The distance from the surface to the maximum melt depth is referred to as the penetration depth s_{pen}. The channel width $B_{Channel}$ is defined as the lateral space through which the melt flows on each side of the capillary.

Ambient air or gases can be trapped in the melt pool and form to a bubble, which can solidify to a pore [6].

Additionally, when the melt solidifies, the resulting weld can contain internal defects such as cracks and undercut. Welds need to be as defect-free as possible for industrial applications, as voids or pores, etc. reduce the strength of the welded part [7]. In industrial applications, quality requirements can be standardized, as in ISO 13,919-1:2021 [8]. Such standards specify the weld seam appearance together with how large and how many internal defects such as pores or cracks are allowed.

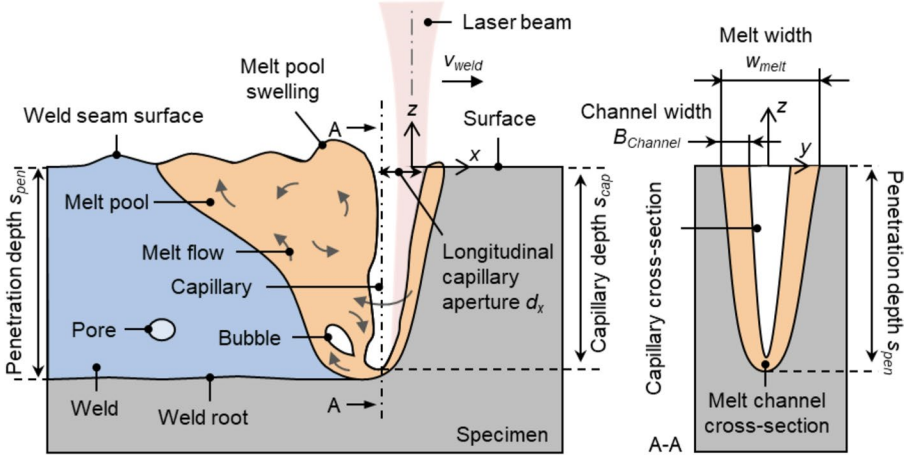


Fig. 1 Sketch of the deep penetration laser welding process

The formation of pores can be linked to a collapse, i.e. a temporal and local partial closing, or other fluctuation of the capillary shape and this is often referred to as capillary-induced pore formation in the literature [6, 9, 10]. As described in [10, 11], the capillary can bulge and contract, and, as it collapses, a cavity can be pinched off to form a bubble filled with a mix of metal vapor and/or ambient gas [12], which subsequently solidifies as a pore. Such pore formation processes occur predominantly at low welding speeds [13, 14], referred to as the "Rosenthal" regime by Fabbro [15]. In this regime the laser generated capillaries are generally narrow, with a high aspect ratio s_{cap}/d_x (the longitudinal capillary aperture diameter at the material surface is d_x) [2, 16]. The contractions and collapses of the capillary result mainly from a disturbance in the interaction between the local evaporation pressure, the vapor flow, the local surface tension, and the static pressure in the surrounding melt pool. A narrow capillary aperture coincides with a smaller radius and is thus linked to high surface tension which can pinch off the capillary if local vapor pressures are too low to withstand it.

In order to reduce the formation of capillary-induced pores in laser welding processes at low welding speeds, collapses and fluctuations of the capillary shape must be avoided. For this to be achieved, the local pressure balances can be addressed by different strategies.

Previously published studies have shown the benefits of the use of nitrogen as a shielding gas for aluminium [6, 12] and steel [17]. Heider et al. [18] and Matsunawa et al. [12] introduced temporal modulation of the laser power to reduce porosity in laser welding. Fetzer et al. and others demonstrated the reduction of porosity achieved by oscillating the laser beam in 2 dimensions on the weld surface during the welding process [19–21]. Others have successfully deployed 3-dimensional oscillation of the laser beam [22, 23], and Hayashi et al. used a twin-spot laser to good effect (TSL) [24]. However, some of these strategies are limited in their application by their unidirectional character and complexity.

Other methods to counter such defects in laser material processing, such as beam shaping techniques, are currently undergoing significant development [25]. One method for generating bespoke intensity distributions involves using concentric double-core fibers in conjunction with a single laser source [26]. These systems generate a ring-shaped intensity distribution around a central spot created via the core of the fiber. Early versions of this approach [27, 28] were technologically limited as the power supplied to the core and the surrounding ring waveguide in the fiber could not be controlled independently. More recent concentric double-core fiber systems [29, 30] can deliver adjustable amounts of laser power to the central core and to the surrounding ring.

Bespoke core-ring intensity distributions have been used to change the laser-material interaction mechanisms in the capillary and the surrounding melt pool in stainless steel [31–33], aluminium [34–36] and copper [29]. Previous studies have demonstrated that the diameter of the capillary aperture and the shape of the weld cross-section can be made to change when welding steel [32, 37–39]. Both the capillary aperture and the weld pool cross section affect the sensitive pressure equilibrium between the vapor capillary and surrounding melt. These changes to the melt pool and the capillary can reduce porosity in the case of specific ratios of core-ring intensity distributions, as shown in different studies on laser welding of aluminium [36, 40, 41]. However, the systems used in the literature describe setups with a range of

different core and ring diameters on the sample surface, which makes it difficult to assign specific phenomena or trends to changes in the ring diameter in isolation.

Within this work, we address this knowledge gap by using different ring diameters with a constant central spot diameter, to influence the melt pool and capillary geometry and the formation of pores in deep penetration laser welding of 1.4301 (X5CrNi18-10, AISI 304) stainless steel at a speed of 3 m/min.

With the aid of synchrotron X-ray high-speed imaging we carried out direct observation of the behaviour of the capillary during the welding process. The high spatial and temporal resolution of the results enabled an in-depth examination of how pores are created and how their formation is affected by changes in laser beam characteristics.

Experimental Setup

A schematic of the experimental setup used is shown in Fig. 2. The sample, made of 1.4301 (X5CrNi18-10, AISI 304) stainless steel, with a thickness t_s of 2 mm, was held, on edge, in a clamping device mounted on a sled that can move in the x-direction with speeds in excess of 20 m/min, see Fig. 2 (1). The moving sample and a stationary laser beam enabled X-ray video investigation of the welding process. The laser system characteristics are given in Table 1.

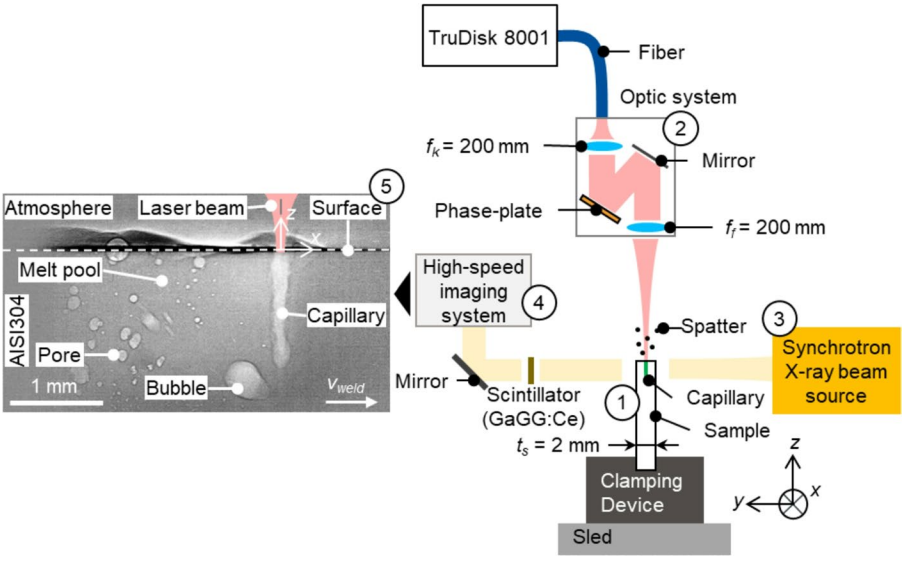


Fig. 2 Schematic of the experimental set-up for synchrotron X-ray imaging. (1) Sample and clamping device on sled, moving in the x-direction (into the page). (2) Optical system with collimation lens f_k=200 mm and focusing lens f_f=200 mm. The collimated beam hits the phase-plate that creates locally adapted phase changes on the beam. (3) Synchrotron X-ray beam source. (4) High-speed imaging system records the capillary shape during the welding process, visualised by the scintillator back-side via a mirror. (5) Frame of an X-ray recording during a welding process, post-processed with a flat-field correction and contrast-enhanced

The laser radiation was transmitted through a conventional glass fiber with a core diameter of 100 µm to special processing optics (Canunda from Cailabs), which were capable of generating intensity distributions with different ring diameters around a central core beam, see Fig. 2 (2). The optics collimated the beam with a lens of 200 mm focal length. The collimated beam was then reflected off a phase-plate with a surface grating that creates phase shifts in the beam [42, 43]. A second, ungrated, mirror then reflects the phase-shifted, collimated, beam to the focussing lens. A focusing lens of 200 mm focal length was used to focus the beam. When focussed, the phase-shifts in the beam create an interference pattern at the focal plane. In these experiments, three phase-plates were used sequentially, creating similar central beam spots and three different diameters of the outer ring. The power distribution between the two portions of the beam was set to 50% to the central spot and 50% to the ring beam in each case. This optical set-up mimics the generation of core and ring energy distributions from three different double core fibre systems. As such intensity distributions would usually be achieved using double-core fibre systems, the central spot will be referred to as the 'core spot' in this work.

The capillary shape was monitored during the welding process using the X-ray imaging system at the Deutsches Elektronen-Synchrotron (DESY) in Hamburg. The X-ray beam, with a photon energy of 74 keV, see Fig. 2 (3), irradiated the sample and was absorbed differently according to the material's thickness and density [44]. The X-ray's high brilliance enabled propagation-based phase contrast, allowing the detection of phase shifts induced by the material, i.e. the liquid-gas boundary of the capillary and the liquid-solid boundary of the melt pool's [45–47]. Behind the sample, a GaGG: Ce scintillator crystal with a thickness of 1.6 mm transformed the X-ray beam into visible light. A high-speed imaging system with a camera (i-SPEED 727 from iX Cameras) and a magnifying optical lens system, captured the scintillator's response (see Fig. 2 (4)) at a 10 kHz framerate with a spatial resolution of 380 pixels/mm and a frame size of 900 × 1600 pixels. A mirror kept the camera out of the beam path to protect its electronics from the X-ray radiation. The resulting images from the X-ray recordings (see Fig. 2 (5)) were post-processed by first applying a flat-field correction to the raw images according to [44], and then the image contrast was adjusted to make the capillary and pores more easily distinguishable from the melt. The sample surface is shown by a dashed line in the figure. The X-ray beams are attenuated to a lesser extent by the capillary, pores and bubbles when propagating through the sample, which is why they appear brighter in the images.

Table 1 Properties and parameters of the laser beam source and the optical system

Parameter	Symbol	Value/unit
Laser system	-	Trumpf TruDisk 8001
Laser type	-	Disk laser
Wavelength of laser beam	λ	1030 nm
Maximum laser power	$P_{Laser,\,max}$	8000 W
Fiber diameter	$d_{f,\,core}$	100 µm
Focal length of collimation lens	f_k	200 mm
Focal length of focusing lens	f_f	200 mm

The beam profiles resulting from the three phase-plates were characterized using a Primes FocusMonitor+. To evaluate the beam propagation profile, the intensity profile in the x-direction was analysed in a range above and below the focal plane. Figure 3 shows the dimensions of the ring and core beams in longitudinal section. The dashed line represents the sample surface at z = 0, the beam propagation direction is from top to bottom. In the interests of brevity and clarity, the three different processing beams will hereafter be referred to as the 'small ring', 'medium ring' and 'large ring'. In the following discussion the ring width w_{ring} of each ring beam refers to the half-difference between its inner diameter $d_{ring,\,in}$ and outer diameter $d_{ring,\,out}$.

In Fig. 3a, for the small ring, the ring radius increases below the focal plane in the -z direction at a rate of 75 µm/mm. The width of the ring beam stays constant at approximately 110 µm as the radius increases. Above the focal plane, the core and ring merge.

In Fig. 3b, for the medium ring geometry, the ring beam radius increases at a rate of 84 µm/mm and the width of the ring beam stays constant at approximately 150 µm.

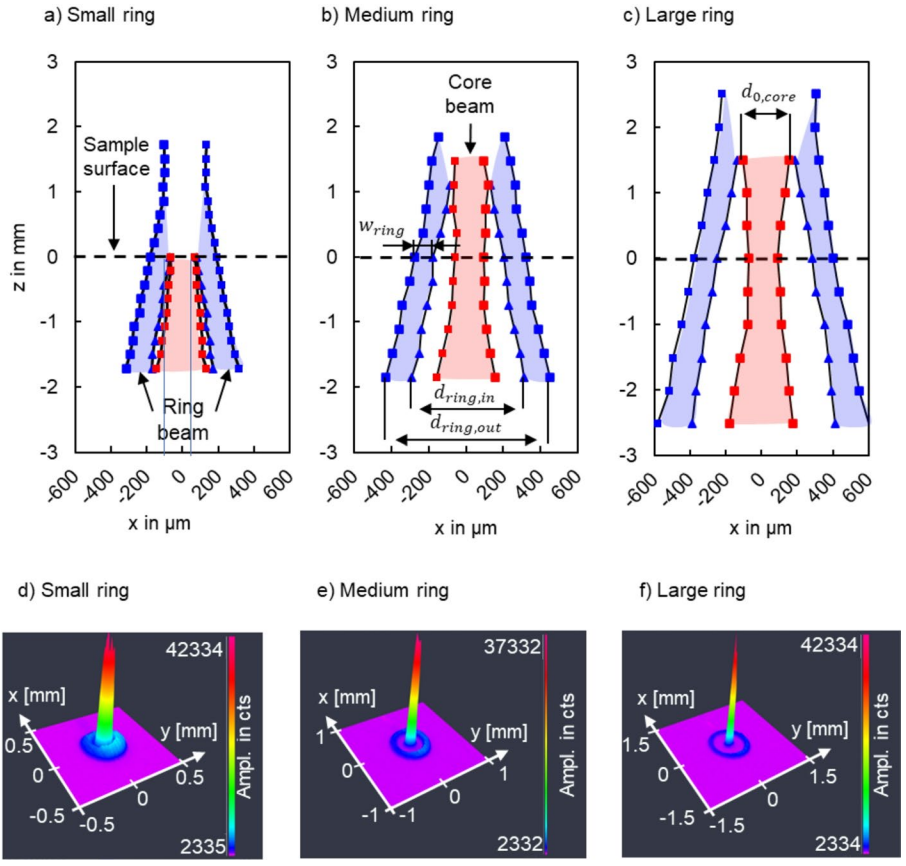


Fig. 3 Dimensions of core (red) and ring (blue) beams from Primes Focus Monitor+ measurements. **a** small ring, **b** medium ring, **c** large ring. The 3 d plane representation of the intensity profile in the focal plane z = 0 for **d** small ring, **e** medium ring, **f** large ring diameter

In Fig. 3c, the large ring radius increases in the -z direction at a rate of 77 µm/mm and the width of the ring beam stays constant at approximately 110 µm as the radius increases.

For each of these rings the core beam has a Gaussian-like profile with the waist at z = 0. The corresponding three-dimensional representations of the intensity profiles in the focal plane at z = 0 are shown in Fig. 3d-f.

Table 2 shows the dimensions of the core spot and ring diameters generated by the different phase-plates at the focal plane (z = 0). The calculated cross-sectional areas of the core beam $A_{0,spot}$ and the ring beam A_{ring} at the focal plane in each case are also shown.

The measurements show that the core spot diameters were $d_{0,core}$ = 150 ± 15 µm. Due to the fact that the X-ray beam was approximately 2 mm in height, the penetration depth was set to 1.5 mm, for direct comparison of results, and to ensure that capillary depth changes were also visible. The total laser power for each configuration of phase-plate was adapted accordingly.

To identify the power required for each phase plate, preliminary power-ramped welds were carried out and the resulting X-ray images were analysed. The laser power required for a penetration depth s_{cap} of approximately 1.5 mm was then identified from the X-ray recordings. Table 3 summarizes the power levels chosen, and gives the resulting average intensities of the core and ring beams for the different ring sizes. It is clear from these figures that the core beam intensity is approximately an order of magnitude higher than that of the ring beam in each case.

Figure 4a shows a typical raw image of an image sequence from the high-speed camera video, and the flat-field corrected image is shown in Fig. 4b.

At the top of the image in Fig. 4b, the melt wake and the surface of the sample, indicated by the white dashed line, can be seen. It is a well-known phenomenon that

Table 2 Beam dimensions on the sample´s surface and the resulting cross-sectional area at the focal plane

Core-ring beam geometry	Core spot diameter in µm	Ring diameter dimensions in µm		Area of central core spot $A_{0,spot}$ in µm²	Area of ring beam A_{ring} in µm² (approx. in each case)
Small ring	$d_{0,core}$ = 135 µm	$d_{ring,in}$ =	150 µm	14.3 · 10³ µm²	90 · 10³ µm²
		$d_{ring,out}$ =	370 µm		
Medium ring	$d_{0,core}$ = 150 µm	$d_{ring,in}$ =	380 µm	17.6 · 10³ µm²	169 · 10³ µm²
		$d_{ring,out}$ =	600 µm		
Large ring	$d_{0,core}$ = 160 µm	$d_{ring,in}$ =	540 µm	20.1 · 10³ µm²	237 · 10³ µm²
		$d_{ring,out}$ =	770 µm		

Table 3 The average laser intensities at the focal plane for the three different core-ring beam geometries

Small ring		Medium ring		Large ring	
Total laser power P_{Laser} 900 W		Total laser power P_{Laser} 1000 W		Total laser power P_{Laser} 1400 W	
Core beam intensity in kW/mm²	Ring beam intensity in kW/mm²	Core beam intensity in kW/mm²	Ring beam intensity in kW/mm²	Core beam intensity in kW/mm²	Ring beam intensity in kW/mm²
31.4	5.0	28.4	2.9	34.8	2.9

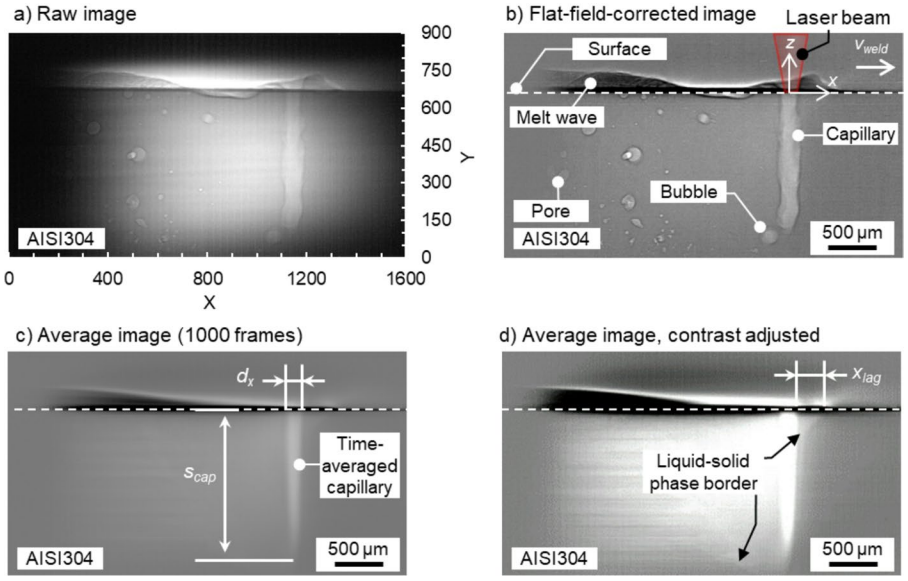


Fig. 4 Synchrotron X-ray images, image processing steps and measurements from the images. **a** Raw image of the recorded image sequence with a resolution of 2.6 µm/pixel, **b** flat-field corrected image **c** average image from 1000 frames **d** average image contrast enhanced

the melt pool can flow upward and the melt at the surface can bulge and swell [48, 49] The location of the laser beam creating the capillary is outlined in red in Fig. 4b. At the tip of the capillary a recently detached bubble can be seen. On the left-hand side of the image several solidified bubbles, i.e. pores, can be seen.

Figure 4c shows an average intensity image AVG of 1000 frames from a flat-field corrected image sequence. In this image the time-averaged shape of the capillary can be seen. The measurements of the capillary such as the depth s_{cap} and longitudinal aperture at the surface d_x are indicated.

By increasing the contrast of the average image, the liquid-solid phase border can be made visible, as shown in Fig. 4d. The contour of the phase border is clearly distinguishable to the right of the capillary, on the left the contour is less visible as bubbles and pores influence the average image, producing horizontal lines. The measurement of the lag between capillary front and melt x_{lag} at the surface of the sample is indicated in this image. It is appropriate to note here that the liquid-solid phase border is much fainter when produced as a printed image (e.g. Fig. 4d) than when observed on a computer screen.

Results & Discussion

In Fig. 5a the average images of a flat field corrected image sequence of each weld with different core-ring-diameter configurations are shown. The white dashed line represents the surface of the samples. Above the images the core-ring beam geometry, with its corresponding ring diameter configuration, is depicted in a schematic at

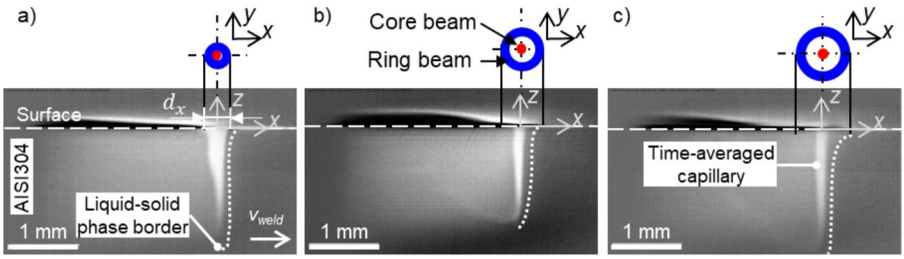


Fig. 5 Average image from 1000 frames of Flat-field-corrected and contrast-adjusted X-ray recordings with the time-averaged capillary shape for different core-ring beam spot geometries. **a** small ring, **b** medium ring, **c** large ring

scale and in plan-view. The contour of the liquid-solid phase border is indicated by the white dotted line. The measurements from these images are presented in Table 4 out of 1000 frames.

It is clear from Table 4 that the capillary top width decreased, and the capillary lag increased, with increasing ring size. The capillary depth was reduced slightly when welding with the medium ring, indicating that the laser power level was set slightly too low for exact comparison with the other two intensity distributions. However, the most important conclusion to be made from Tables 2 and 4 is that, in the case of the small ring beam, the outer ring diameter (320 µm) is small enough that the radiation contributions from both the core and the ring are acting together to create the capillary (top width approx. 330 µm). In the cases of the medium and large rings, the core beam alone creates the capillary and the ring beams act as pre- and post-heating inputs.

Although there are minor differences between the capillary depths noted for each of the ring sizes in Table 4, these are considered to be too small to affect the findings of this experimental program [50].

Melt Pool Dimensions

The influence of the different ring diameters on the resulting weld can be seen in the cross-sections displayed in Fig. 6. These typical sections allow for investigation of the penetration depth s_{pen} from the surface to the weld seam root, and the melt pool width w_{melt} at the top of the weld (z=0). The capillary aperture d_x is marked in orange, and the top surface channel width $B_{Channel}$ is indicated. In the case of the weld seam with the large ring, see Fig. 6c, the proximity of the weld to one side of the sample results in greater heat accumulation, which led to a slightly asymmetrical cross-section.

Table 4 Capillary and melt pool dimensions

	Capillary depth s_{cap} in mm	Longitudinal capillary aperture d_x in µm	Aspect ratios$_{cap}$/d_x	Capillary/melt lag x_{lag} in µm
Small ring	1.5±0.06	330±20	4.54±0.5	130±20
Medium ring	1.28±0.06	190±20	6.74±1.1	220±20
Large ring	1.62±0.06	160±20	9.31±2.0	320±20

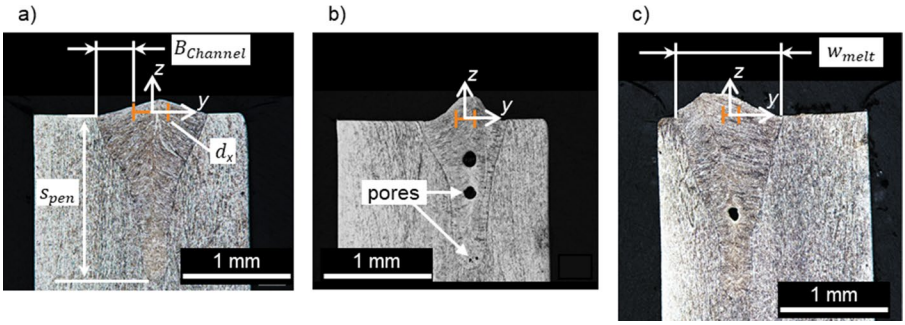


Fig. 6 Cross sections of the welds produced with different ring diameters, **a** small ring, **b** medium ring, **c** large ring

Table 5 summarises the dimensional results taken from the cross sections and, in combination with the measurements of the capillary diameter from Table 4, the top surface channel widths $B_{Channel}$, see Fig. 1, have been determined. For the estimation of $B_{Channel}$ it has been assumed that the capillary aperture is approximately circular in cross section at this low welding speed.

The images show typical shapes of the laser weld seam cross-section, with a widening of the seam at the sample surface and a narrowing of the width with increasing depth. Although there are strong similarities between the appearance of the weld cross sections, it is important to notice that at the top of the weld the channel width $B_{Channel}$ has been increased by over 20% in the case of the large ring compared to the small ring. This measurement is an indication of the size of the gap between the capillary and the solid-liquid interface through which all the melt must flow. An increase in this gap for welds of similar cross-section is linked to a decrease in melt velocities around the capillary in that region [5]. Once again, the slight differences between capillary depths are considered to be negligible are far as the following discussion is concerned [41].

Capillary Dimensions

Figure 7a presents the profiles of the capillaries in the direction of travel determined from the X-ray images, and Fig. 7b provides information about the capillary diameter in the x-direction as a function of depth.

The profiles of the time-averaged capillaries for the medium and large rings are very similar, with almost parallel-sided walls. The lack of laser power reduced the depth of the medium ring capillary slightly. The profile of the capillary with the small

Table 5 Dimensions of cross-sections for different ring diameters

	Penetration depth s_{pen} in mm	Melt pool width w_{melt} in mm	Channel width $B_{Channel}$ in mm
Small ring	1.52	1.04	0.355±0.02
Medium ring	1.39	0.82	0.315±0.02
Large ring	1.72	1.02	0.430±0.02

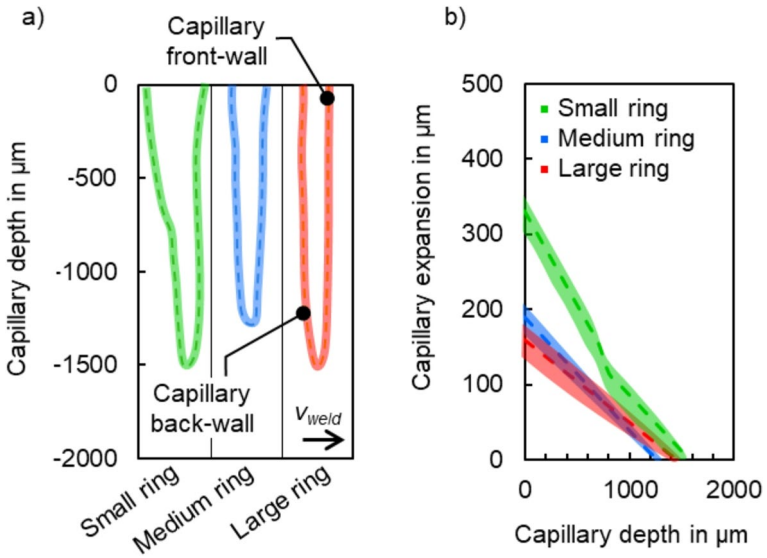


Fig. 7 **a** capillary contours at scale, **b** capillary diameter as a function of capillary depth

ring shows a more flared and open profile, with twice the expansion of the capillary at the surface as the other ring configurations. This open geometry provides beneficial conditions, such as improvements to outflowing vapor flow, for less gas to become trapped within the weld, and this is supported by the weld porosity measurements in the next section.

Weld Porosity Measurements

A pore in a weld is a result of solidified bubbles of trapped ambient air, shielding gas or vapor in the melt pool, often caused by the collapse of a capillary [12].

X-ray images and longitudinal sections were used to examine the weld seams for pores, as shown in Fig. 8. The X-ray scans were created in post-processing by overlaying images from the original X-ray recording of the solidified melt and compensating for pixel shifts between frames. One major advantage of this technique, compared to longitudinal cut sections, is that all the pores above a certain size, in every y-plane, can be seen. The resolution of the camera system was 380 pixels/mm, or 2.6 µm/pixel, limiting the optically resolvable pores to those bigger than 5 µm in diameter. The matching center-line longitudinal cross section of each sample is shown directly below its X-ray scan. The red circles in the X-ray scan image and the longitudinal section mark the same pore in both images. It should be noted that the pore diameter in the longitudinal section does not represent the actual pore diameter unless the section happens to cut through the center of the pore. However, in comparison to the X-ray Scan, the longitudinal section shows the melt penetration depth more clearly, and the dotted line plots the profile of the weld penetration depth s_{pen}. On the right, close-ups of the X-ray scans are shown. The X-ray scans of the complete weld seams can be downloaded from DARUS [51].

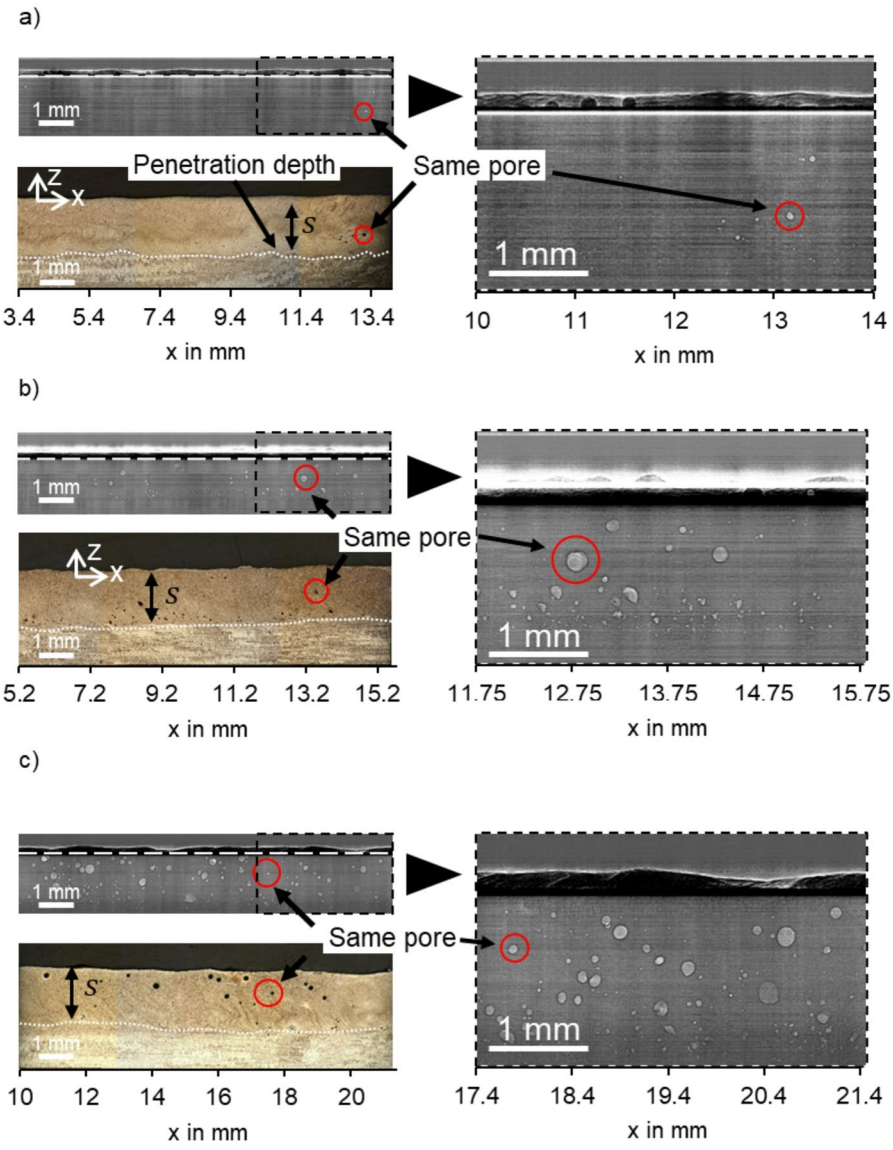


Fig. 8 Porosity in the welds. The grayscale image shows the X-ray scan, where pores appear as a lighter grey. Below the X-ray scan, the appropriate longitudinal section can be seen. The red circles mark the position of identical pores in both images. **a** Small ring, **b** Medium ring, **c** Large ring. The X-ray scans displayed are downloadable from DARUS [51]

Figure 8a shows that when welding with the small ring the pores are small and infrequent. A total of 4 pores of approximately 80 µm in diameter were counted in a 10 mm length of this weld. Smaller pores with sizes of 30 µm or lower were found at the level of the capillary tip. The pore fraction is below 0.15%, calculated by dividing the cumulative pore area by the area of the weld area in the X-ray scan. Pore

fractions measured from X-ray photographs give higher values than those estimated from cross sections because all the pores in the weld are counted and they are all measured at their full diameter. Figure 8b, shows that when welding with the medium ring, more frequent and larger pores can be seen. In a weld length of 10 mm a total of 234 pores were counted. The biggest pores are approximately 200 µm in diameter and are positioned in the middle of the penetration depth. Smaller pores with sizes of up to 50 µm can be seen at the level of the capillary tip. The pore fraction in this case is 1.4%.

In Fig. 8c, when welding with the large ring, in a 10 mm section of weld a total of 242 pores were counted. The number is similar to that for Fig. 8b, but the pores are generally larger, with the biggest pores reaching 320 µm in diameter. The pore fraction is 3.4%, confirming that bigger pores are present. Furthermore, non-spherical pores can be seen, the formation mechanisms of which will be discussed in Sec 8.

The pore population measurements are summarized in Table 6.

The Influence of Ring Diameter on the Pore Formation Process

For this investigation the X-ray recordings were analyzed to investigate the mechanisms leading to the formation of a pore. This includes the pinch-off of a bubble from the capillary, its movement in the melt pool and the transition to a pore in the solidified melt.

Figure 9 shows one of the basic principles of pore formation during the laser welding process. The tip of the capillary occasionally breaks away due to a bulging and necking event. In the case shown here, welded with the small ring, it is clear that the bubble was primarily filled with metal vapor which condenses during cooling to result in a very small pore. As we shall see later, bubbles which contain a substantial amount of air do not shrink to the same extent.

Figure 10 shows the X-ray image sequence detailing the creation of pores from the small ring capillary starting at $t_{0,}$ which corresponds to t = 270.50 ms into the welding process or a welding distance of 10.375 mm. Note; the dark spot at the right-hand side of the image is an airborne spatter particle. The capillary opening is generally enlarged in its upper section due to the additional energy input from the small ring. The time interval between the first and final images shown here is 0.7 ms, equivalent to a welding distance of 35 µm.

At t_0 + 0.30 ms a bulging event near the middle of the capillary is visible, followed 10 ms later by a constriction in capillary diameter. The location of the constriction s_{con} is 880 µm below the sample surface. As a result, only a small volume of the capillary is separated from its bottom tip to create a bubble, and this rapidly shrinks as the metal vapor inside condenses (t_0 + 0.70 ms). The small amount of remaining

Table 6 Analysis of pore formation from X-ray scans for different core-ring geometries

	Pores per mm welding distance in mm^{-1}	Biggest pore diameter in µm	Area pore fraction in %
Small ring	0.13	80	< 0.15
Medium ring	24.2	200	1.4
Large ring	23.4	320	3.4

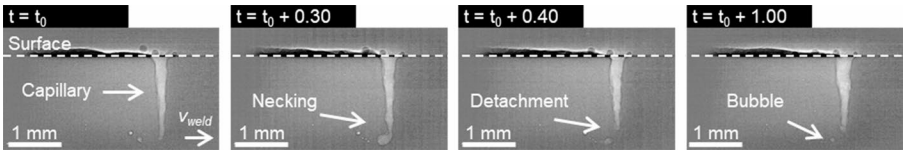


Fig. 9 Formation of small bubbles due to necking events at the capillary tip when welding with the small ring [51]

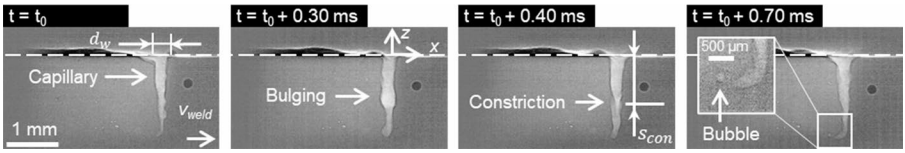


Fig. 10 Pore formation process when welding with a small ring diameter [51]

atmospheric gas within the bubble then results in the formation of a small pore. This cycle fits to the 'capillary bulging – bubble separation' event noted in [52].

Using the small diameter ring increases the amount of vaporization at the top of the capillary. This expands the aperture at the top and allows any trapped gas to leave the are more easily.

Figure 11 shows the process of the formation of pores when welding with the medium ring. The image sequence starts at t_0, corresponding to t = 153.90 ms into the welding process or a welding distance of 7.695 mm. The capillary in this case is generally narrower than the one created by the small ring beam because the ring beam is too broad in diameter to enter the capillary. Once again there is a bulging-constriction event, but in this case, it takes place close to the top of the capillary, where the bulging event is more likely to capture atmospheric air. This idea of enhanced air entrapment is supported by the fact that the bubble ejected from the bottom of the capillary is larger than the one ejected by the small ring beam, and it shrinks less due to vapor condensation. To characterize the bulging dimension, the area of the cross-section of the capillary at $t_0 + 0.40$ ms was measured as 0.289 mm², an increase of 60%, compared to the capillary cross-section area at t_0 which was 0.176 mm². If the capillary is assumed to be approximately circular in cross section, the increase in its volume will be considerably greater than the cross-sectional increase.

Figure 12 shows the process of the formation of pores when welding with the large ring.

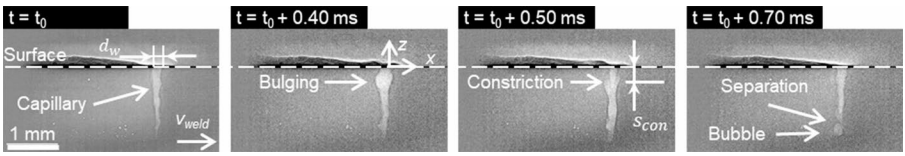


Fig. 11 Pore formation process when welding with a medium ring diameter [51].

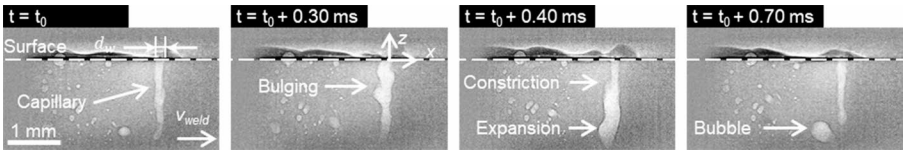


Fig. 12 Pore formation process when welding with a large ring diameter [51].

The image sequence starts at t_0, corresponding to t = 523.80 ms into the welding process and a distance of 26.29 mm from the start of the weld. Here, the capillary is rather narrow and slightly deformed. On the left-hand side of the image, previously generated pores are visible. At $t_0 + 0.30$ ms a bulging of the capillary can be seen, which extends to its full depth. As a result of the bulging event the cross-section area of the capillary increases from approximately 0.265 mm² to 0.5 mm².

The bulging event is followed by a constriction of the capillary at $t_0 + 0.40$ ms. The constriction effect begins at the top of the capillary and progresses downwards, presumably trapping atmospheric gases. The location of the constriction s_{con} is 250 µm below the surface. At the capillary tip, the expansion indicated reaches 380 µm at its widest point.

At $t_0 + 0.70$ ms a bubble can be seen separating itself from the capillary bottom. The diameter of the bubble was measured as 400 µm. After the bubble is created, it moves around in the melt pool before it eventually solidifies. As was the case for the medium ring pore, the lack of condensation shrinkage indicates that this bubble is primarily filled with air.

From the above there are clear indications that having a ring beam narrow enough to enter the capillary and keep it open inhibits the formation of pores formed when air becomes trapped in the capillary. The use of larger diameter ring sources had the effect of increasing the melt front/capillary lag x_{melt}, which may increase the susceptibility of the capillaries to bulging-necking events which trap air and result in pore formation.

Beneficial effects of the added ring beam to pore formation were achieved when laser power from the ring beam was absorbed at the capillary inner wall. As a rule, to check if this condition is achieved, the ratio between the core beam only capillary aperture and inner ring beam diameter $d_x/d_{ring,\ in}$ can be used. At ratios greater than one, the rays reach in the capillary, and at ratios below 1, the ring beam is absorbed at the surface.

The Formation of non-spherical Pores

Most bubbles in liquids are approximately spherical, and give rise to spherical pores when they solidify. A small proportion of the larger pores in laser welds are, however, profoundly non-spherical. Such features are not just of purely academic interest as non-spherical pores are likely to be more serious stress raisers than their spherical counterparts. This phenomenon can be explained with the help of Fig. 13, which shows the evolution of such a pore. In this work the only bubbles large enough to solidify as non-spherical pores were generated when using the medium and large rings.

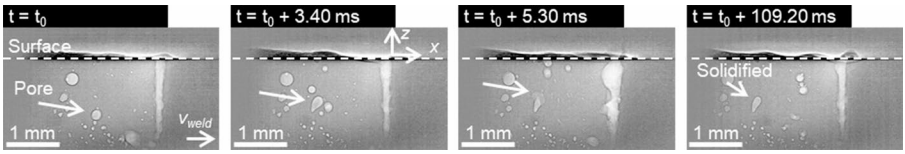


Fig. 13 Formation of non-spherical pore. A spherical bubble at t_0 (t = 211.50 ms) becomes anchored to the encroaching solidification front. The buoyancy of the non-anchored remainder of the bubble causes it to elongate before the whole pore solidifies [51].

Figure 13 shows the position of a large bubble created during the medium ring welding process at t_0, corresponding to t = 211.50 ms into the welding process, at which point it has its natural, spherical shape. At t_0 + 3.40 ms, the solidification front overtakes the rear part of the bubble (i.e., low on the left-hand side) and anchors this area to the solidified weld. For several milliseconds after this the side of the bubble furthest from the encroaching solidification front is still mobile and surrounded by liquid. The buoyancy of this anchored half-bubble, combined with the force of the local melt flow, make it extend into a non-spherical shape. Eventually, by t_0 + 109.20 ms in this case, the whole bubble is overtaken by the solidification front and it solidifies as a non-spherical pore. This 'tethered bubble plus partial mobility' phenomenon requires a certain amount of time for the solidification front to cross the bubble/pore, which is why this process only applies to larger bubbles. A comparable behavior in copper was observed in [52].

Another mechanism that can give rise to non-spherical pores is the agglomeration of two or more bubbles, one of which may already be anchored by partial solidification. A merging process of this type is presented in Fig. 14. At t_0 two separate bubbles are indicated in the image, with both bubbles already anchored by partial solidification. At t_0 + 0.20 ms the non-anchored parts of the two bubbles merge. At t_0 + 9.50 ms the merged bubbles are solidified as a non-spherical pore.

The non-spherical pore generation mechanisms described above are not ring-core specific. They are undoubtedly true for all laser welding processes when relatively large bubbles are created in the melt and solidify as non-spherical pores. The basic principle will also hold true for many other welding processes.

The results presented here are, of course, for a specific parameter set. However, the fundamental mechanisms of pore formation and capillary collapse will apply for all such high-aspect ratio welding processes [53]. The beneficial effects of small ring beams on reducing pore formation at other welding speeds and laser powers is a subject to be explored in future research.

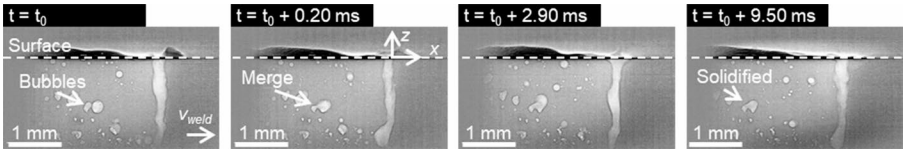


Fig. 14 Agglomeration of two bubbles to form a non-spherical pore [51].

Conclusions

The following conclusions can be drawn from this work:
Effect of ring beam diameter on capillary behaviour.

- Laser beams shaped to a narrow ring can penetrate into the capillary with the core beam and enlarge its upper section. This produces a more flared geometry, which reduces atmospheric gas entrapment and pore formation.
- The longitudinal capillary aperture was largest with the small ring at 330 µm, and shrunk to 190 µm with the medium ring beam, to ultimately 160 µm with the large ring beam diameter.
- Wide rings do not deliver energy directly into the capillary. Instead, they act as pre- and post-heating sources and modify the melt geometry.

Capillary dynamics and gas entrapment.

- Pressure imbalances within the capillary can cause bulging or constriction events, which may draw in atmospheric gases (air or shielding gas).
- When a narrow ring beam keeps the upper capillary section open, constriction events occur near the bottom of the capillary. In this case, only a small amount of gas, primarily metal vapor, is trapped, resulting in very small pores.
- If the ring beam is too wide to transfer energy into the capillary, constriction begins near the top. This promotes significant atmospheric gas entrapment and leads to the generation of larger pores.

Pore morphology.

- Large bubbles within the melt solidify gradually as the solidification front passes through them. During this process, they may deform and form non-spherical pores.
- Non-spherical pores can also result from the coalescence of two or more bubbles.

Pore characteristics.

- For the small ring diameter, 0.13 pores per mm with an average diameter of 80 µm were present, at a pore fraction of below 0.15%.
- For the medium ring diameter, 6.7 pores per mm with an average diameter of 200 µm were present, at a pore fraction of below 1.4%.
- For the large ring diameter, 9.3 pores per mm with an average diameter of 320 µm were present, at a pore fraction of below 3.4%.

(Partially) Supported by the InnovationCampus Future Mobility funded by the Baden-Württemberg Ministry of Science, Research and Arts.
The presented investigations were carried out within the cooperation “Laser Meets Synchrotron” (www.laser-meets-synchrotron.de). The experimental setup and its operation were funded by the Deutsche Forschungsgemeinschaft e.V. (DFG, German Research Foundation) within the framework of the Collaborative

Research Centre SFB1120-236616214 “Bauteilpräzision durch Beherrschung von Schmelze und Erstarrung in Produktionsprozessen”. The experiments were carried out in cooperation with Helmholtz-Zentrum Hereon in Hamburg at Beamline P07 of DESY PETRA III as part of proposal BAG-20211050 and we would like to thank F. Beckmann, J. Moosmann and all people involved for their support.
We would like to thank Cailabs for the unrestricted provision of the optics including the Canunda-Beam-Shaping-module for our research use.
Declarations.

Author Contributions **Felix Zaiß** : Conceptualization, Methodology, Writing (original draft), Investigation, Data Curation, Supervision. **John Powell** : Writing (review & editing), Supervision, Methodology, Validation. **Michael Haas** : Writing (review & editing), Investigation, Methodology, Data Curation. **Christian Diegel** : Writing (review & editing), Investigation. **Klaus Schricker** : Writing (review & editing). **Jean Pierre Bergmann** : Writing (review & editing). **Christoph Spurk** : Writing (review & editing). **Marc Hummel** : Writing (review & editing). **Alexander Olowinsky** : Funding acquisition. **Felix Beckmann** : Data Curation. **Julian Moosmann** : Writing (review & editing). **Christian Hagenlocher** : Supervision, Writing (review & editing). **Thomas Graf** : Writing (review & editing).

Funding Open Access funding enabled and organized by Projekt DEAL. The presented work was funded by the Deutsche Forschungsgemeinschaft (DFG, German Research Foundation) – 503306266.

Data Availability X-ray recordings are accessible on [https://darus.uni-stuttgart.de/dataset.xhtml?persistentId=doi:10.18419/darus-4356](https:/darus.uni-stuttgart.de/dataset.xhtml? persistentId=doi:10.18419/darus-4356).

Declarations

Ethical Approval Not applicable.

Competing interests The authors declare no competing interests.

Open Access This article is licensed under a Creative Commons Attribution 4.0 International License, which permits use, sharing, adaptation, distribution and reproduction in any medium or format, as long as you give appropriate credit to the original author(s) and the source, provide a link to the Creative Commons licence, and indicate if changes were made. The images or other third party material in this article are included in the article’s Creative Commons licence, unless indicated otherwise in a credit line to the material. If material is not included in the article’s Creative Commons licence and your intended use is not permitted by statutory regulation or exceeds the permitted use, you will need to obtain permission directly from the copyright holder. To view a copy of this licence, visit http://creativecommons.org/licenses/by/4.0/.

References

1. Arata, Y., Abe, N., Oda, T.: Beam hole behaviour during laser beam welding. In: International Congress on Applications of Lasers & Electro-Optics, pp. 59–66. Laser Institute of America, Los Angeles, California, USA (1983)
2. Cunningham, R., Zhao, C., Parab, N., Kantzos, C., Pauza, J., Fezzaa, K., Sun, T., Rollett, A.D.: Keyhole threshold and morphology in laser melting revealed by ultrahigh-speed x-ray imaging. Science. **363**, 849–852 (2019). https://doi.org/10.1126/science.aav4687
3. Solana, P., Negro, G.: A study of the effect of multiple reflections on the shape of the keyhole in the laser processing of materials. J. Phys. D: Appl. Phys. **30**, 3216–3222 (1997). https://doi.org/10.1088/0022-3727/30/23/006
4. Laser remote welding for series production | PRECITEC: https://www.precitec.com/laser-welding/products/scanner-welding/

5. Beck, M.: Modellierung des Lasertiefschweißens. Teubner, Stuttgart (1996)
6. Seto, N., Katayama, S., Matsunawa, A.: Porosity formation mechanism and suppression procedure in laser welding of aluminium alloys. Weld. Int. **15**, 191–202 (2001). https://doi.org/10.1080/09507110109549341
7. He, E., Liu, J., Lee, J., Wang, K., Politis, D.J., Chen, L., Wang, L.: Effect of porosities on tensile properties of laser-welded Al-Li alloy: An experimental And modelling study. Int. J. Adv. Manuf. Technol. **95**, 659–671 (2018). https://doi.org/10.1007/s00170-017-1175-3
8. DIN EN ISO 13919-: 1:2020-03, Elektronen- und Laserstrahl-Schweißverbindungen_- Anforderungen und Empfehlungen für Bewertungsgruppen für Unregelmäßigkeiten_- Teil_1: Stahl, Nickel, Titan und deren Legierungen (ISO_13919-1:2019); Deutsche Fassung EN_ISO_13919-1:2019. https://www.dinmedia.de/de/-/-/311429259
9. Lee, J.Y., Ko, S.H., Farson, D.F., Yoo, C.D.: Mechanism of keyhole formation and stability in stationary laser welding. J. Phys. D: Appl. Phys. **35**, 1570 (2002). https://doi.org/10.1088/0022-3727/35/13/320
10. Xu, J., Rong, Y., Huang, Y., Wang, P., Wang, C.: Keyhole-induced porosity formation during laser welding. J. Mater. Process. Technol. **252**, 720–727 (2018). https://doi.org/10.1016/j.jmatprotec.2017.10.038
11. Fetzer, F., Hu, H., Berger, P., Weber, R., Graf, T.: Pores in laser beam welding: Generation mechanism and impact on the melt flow. In: Kaierle, S., Heinemann, S.W. (eds.) High-Power Laser Materials Processing: Applications, Diagnostics, and Systems VII, p. 12. SPIE, San Francisco, United States (2018)
12. Matsunawa, A., Mizutani, M., Katayama, S., Seto, N.: Porosity formation mechanism and its prevention in laser welding. Weld. Int. **17**, 431–437 (2003). https://doi.org/10.1533/wint.2003.3138
13. Fetzer, F., Hagenlocher, C., Weber, R.: High Power, High Speed, High Quality. LTJ **15**, 28–31 (2018). https://doi.org/10.1002/latj.201800017
14. Huang, L., Hua, X., Wu, D., Ye, Y.: Role of welding speed on keyhole-induced porosity formation based on experimental and numerical study in fiber laser welding of al alloy. Int. J. Adv. Manuf. Technol. **103**, 913–925 (2019). https://doi.org/10.1007/s00170-019-03502-x
15. Fabbro, R.: Melt pool and keyhole behaviour analysis for deep penetration laser welding. J. Phys. D: Appl. Phys. **43**, 445501 (2010). https://doi.org/10.1088/0022-3727/43/44/445501
16. Zhao, C., Parab, N.D., Li, X., Fezzaa, K., Tan, W., Rollett, A.D., Sun, T.: Critical instability at moving keyhole tip generates porosity in laser melting. Science **370**, 1080–1086 (2020). https://doi.org/10.1126/science.abd1587
17. Hafez, K.M.: The influence of shielding gases on keyhole-induced porosity and nitrogen absorption in SS 304 stainless steel fiber laser welds. Int. J. Adv. Manuf. Technol. **127**, 1887–1894 (2023). https://doi.org/10.1007/s00170-023-11665-x
18. Heider, A., Stritt, P., Hess, A., Weber, R., Graf, T.: Process stabilization at welding copper by laser power modulation. Phys. Procedia. **12**, 81–87 (2011). https://doi.org/10.1016/j.phpro.2011.03.011
19. Fetzer, F., Sommer, M., Weber, R., Weberpals, J.-P., Graf, T.: Reduction of pores by means of laser beam Oscillation during remote welding of AlMgSi. Opt. Lasers Eng. **108**, 68–77 (2018). https://doi.org/10.1016/j.optlaseng.2018.04.012
20. Wu, M., Luo, Z., Li, Y., Liu, L., Ao, S.: Effect of oscillation modes on weld formation and pores of laser welding in the horizontal position. Optics & Laser Technology **158**, 108801 (2023). https://doi.org/10.1016/j.optlastec.2022.108801
21. Wang, L., Gao, M., Zhang, C., Zeng, X.: Effect of beam oscillating pattern on weld characterization of laser welding of AA6061-T6 aluminum alloy. Mater. Design. **108**, 707–717 (2016). https://doi.org/10.1016/j.matdes.2016.07.053
22. Wu, Q., Xiao, R.S., Zou, J.L., Xu, J.J.: Weld formation mechanism during fiber laser welding of aluminum alloys with focus rotation and vertical Oscillation. J. Manuf. Process. **36**, 149–154 (2018). https://doi.org/10.1016/j.jmapro.2018.10.004
23. Liu, Z., Zhang, P., Yan, M., Yu, Z., Tian, Y., Wu, D.: Study of mode transition in three-dimensional laser beam oscillating welding of aluminum alloy. Journal of Materials Processing Technology **303**, 117490 (2022). https://doi.org/10.1016/j.jmatprotec.2022.117490
24. Hayashi, T., Matsubayashi, K., Katayama, S., Abe, N., Matsunawa, A., Ohmori, A.: Reduction mechanism of porosity in tandem twin-spot laser welding of stainless steel. Weld. Int. **17**, 12–19 (2003). https://doi.org/10.1533/wint.2003.3050
25. Hansen, K.S., Kristiansen, M., Olsen, F.O.: Beam Shaping to Control of Weldpool Size in Width and Depth. Physics Procedia **56**, 467–476 (2014). https://doi.org/10.1016/j.phpro.2014.08.150
26. Nagel, F., Brömme, L., Bergmann, J.P.: Description of the influence of two laser intensities on the spatter formation on laser welding of steel. Procedia CIRP. **74**, 475–480 (2018). https://doi.org/10.1016/j.procir.2018.08.147

27. Speker, N., Haug, P., Feuchtenbeiner, S., Hesse, T., Havrilla, David, L.: BrightLine weld-spatter reduced high speed welding with disk lasers. Presented at the January 1 (2018)
28. Feuchtenbeiner, S., Dubitzky, W., Hesse, T., Speker, N., Haug, P., Seebach, J., Hermani, J.-P., Havrilla, D.: Beam shaping BrightLine Weld: latest application results. In: High-Power Laser Materials Processing: Applications, Diagnostics, and Systems VIII. pp. 207–214. SPIE (2019) https://doi.org/10.1117/12.2509560
29. Punzel, E., Hugger, F., Dörringer, R., Dinkelbach, T.L., Bürger, A.: Comparison of different system technologies for continuous-wave laser beam welding of copper. Procedia CIRP. **94**, 587–591 (2020). https://doi.org/10.1016/j.procir.2020.09.081
30. Coherent: Adjustable Ring Mode (ARM) Faserlaser – HighLight FL-ARM. https://www.coherent.com/de/lasers/fiber/highlight-fl-arm
31. Wang, L., Mohammadpour, M., Yang, B., Gao, X., Lavoie, J.-P., Kleine, K., Kong, F., Kovacevic, R.: Monitoring of keyhole entrance and molten pool with quality analysis during adjustable ring mode laser welding. Appl. Opt. **59**, 1576 (2020). https://doi.org/10.1364/AO.383232
32. Wang, L., Mohammadpour, M., Gao, X., Lavoie, J.-P., Kleine, K., Kong, F., Kovacevic, R.: Adjustable ring mode (ARM) laser welding of stainless steels. Opt. Lasers Eng. **137**, 106–360 (2021). https://doi.org/10.1016/j.optlaseng.2020.106360
33. Wang, L., Gao, X., Kong, F.: Keyhole dynamic status and spatter behavior during welding of stainless steel with adjustable-ring mode laser beam. J. Manuf. Process. **74**, 201–219 (2022). https://doi.org/10.1016/j.jmapro.2021.12.011
34. Punzel, E., Hugger, F., Dinkelbach, T., Bürger, A.: Influence of power distribution on weld seam quality and geometry in laser beam welding of aluminum alloys. Procedia CIRP. **94**, 601–604 (2020). https://doi.org/10.1016/j.procir.2020.09.086
35. Maina, M.R., Okamoto, Y., Okada, A., Närhi, M., Kangastupa, J., Vihinen, J.: High surface quality welding of aluminum using adjustable ring-mode fiber laser. J. Mater. Process. Technol. **258**, 180–188 (2018). https://doi.org/10.1016/j.jmatprotec.2018.03.030
36. Hollatz,S., Hummel, M., Lach, M., Olowinsky, A., Gillner, A., Häfner, C., Beckmann, F., Moosmann, J.: Influence of ring-shaped laser beam during welding of AW-5083 and AW-6082. In: High-Power Laser Materials Processing: Applications, Diagnostics, and Systems XII. pp. 80–89. SPIE (2023). https://doi.org/10.1117/12.2649092
37. Jarwitz, M., Lind, J., Weber, R., Graf, T.: Influence of superimposed intensity distributions on the welding process and the spatter behavior during laser welding of steel. In: Proceedings of the Fourth International WLT-Conference on Lasers in Manufacturing. AT-Fachverlag, München (2019)
38. Trumpf, TRUMPF Laser Technology Center: : BrightLine Weld: Perfect welding results in record time. https://www.trumpf.com/filestorage/TRUMPF_CA/user_upload/TRUMPF_BrightLine_Weld.pdf
39. Mohammadpour, M., Wang, L., Kong, F., Kovacevic, R.: Adjustable ring mode and single beam fiber lasers: A performance comparison. Manufacturing Letters **25**, 50–55 (2020). https://doi.org/10.1016/j.mfglet.2020.07.003
40. Shin, J., Kang, S., Hyun, K., Ji, H.: In-depth characterization of an aluminum alloy welded by a dual-mode fiber laser. J. Mater. Res. Technol. **18**, 2910–2921 (2022). https://doi.org/10.1016/j.jmrt.2022.03.187
41. Yang, L., Geng, S., Jiang, P., Wang, Y., Xiong, J.: Investigation on the keyhole/molten pool dynamic behavior during adjustable ring-mode laser welding of medium-thick aluminum alloy. International Journal of Thermal Sciences **196**, 108723 (2024). https://doi.org/10.1016/j.ijthermalsci.2023.108723
42. Bayol, J.: Development of an MPLC-based laser head. PhotonicsViews **18**, 54–58 (2021). https://doi.org/10.1002/phvs.202100060
43. Meunier, M., Lemaitre, D., Lucas, A., Vernaz-Gris, P., Cornee, R., Gusachenko, I., Pallier, G., Laurensot, E., Pinel, O.: High throughput laser beam welding with 16 kW 1.03 µm annular beam shaping. In: High-Power Laser Materials Processing: Applications, Diagnostics, and Systems X. p. 116790B. SPIE (2021) https://doi.org/10.1117/12.2584062
44. Abt, F., Boley, M., Weber, R., Graf, T., Popko, G., Nau, S.: Novel X-ray System for in-situ Diagnostics of Laser Based Processes – First Experimental Results. Physics Procedia **12**, 761–770 (2011). https://doi.org/10.1016/j.phpro.2011.03.095
45. Miyagi, M., Kawahito, Y., Kawakami, H., Shoubu, T.: Dynamics of solid-liquid interface and porosity formation determined through x-ray phase-contrast in laser welding of pure al. J. Mater. Process. Technol. **250**, 9–15 (2017). https://doi.org/10.1016/j.jmatprotec.2017.06.033
46. Kawahito, Y., Wang, H.: In-situ observation of laser manufacturing with X-ray technique. Synchrotron Radiation News. **32**, 14–19 (2019). https://doi.org/10.1080/08940886.2019.1582283

47. Gureyev, T.E., Mayo, S.C., Myers, D.E., Nesterets, Y., Paganin, D.M., Pogany, A., Stevenson, A.W., Wilkins, S.W.: Refracting Röntgen's rays: Propagation-based x-ray phase contrast for biomedical imaging. Journal of Applied Physics (2009). https://doi.org/10.1063/1.3115402
48. Kawahito, Y., Uemura, Y., Doi, Y., Mizutani, M., Nishimoto, K., Kawakami, H., Tanaka, M., Fujii, H., Nakata, K., Katayama, S.: Elucidation of effect of welding speed on melt flows in high-brightness and high-power laser welding of stainless steel on basis of three-dimensional X-ray transmission in-situ observation. QUARTERLY JOURNAL OF THE JAPAN WELDING SOCIETY **33**, 13–19 (2015). https://doi.org/10.2207/qjjws.33.13
49. Katayama, S., Kobayashi, Y., Mizutani, M., Matsunawa, A.: Effect of vacuum on penetration and defects in laser welding. J. Laser Appl. **13**, 187–192 (2001). https://doi.org/10.2351/1.1404413
50. Kaufmann, F., Schrauder, J., Hummel, M., Spurk, C., Olowinsky, A., Beckmann, F., Moosmann, J., Roth, S., Schmidt, M.: Towards an Understanding of the challenges in laser beam welding of copper – Observation of the laser-Matter interaction zone in laser beam welding of copper and steel using in situ synchrotron X-Ray imaging. Lasers Manuf. Mater. Process. **11**, 37–76 (2024). https://doi.org/10.1007/s40516-023-00225-6
51. Zaiß, F.: Supplementary data: Core-ring laser welding: The influence of ring diameter on the capillary collapse and the formation of pores in the resulting weld, :https://doi.org/10.18419/darus-4356
52. Schricker, K., Schmidt, L., Friedmann, H., Diegel, C., Seibold, M., Hellwig, P., Fröhlich, F., Bergmann, J.P., Nagel, F., Kallage, P., Rack, A., Requardt, H., Chen, Y.: Characterization of keyhole dynamics in laser welding of copper by means of high-speed synchrotron X-ray imaging. Procedia CIRP. **111**, 501–506 (2022). https://doi.org/10.1016/j.procir.2022.08.079
53. Florian, F., Peter, B., Haoyue, H., Rudolf, W., Thomas, G.: Pores in laser beam welding: generation mechanism and impact on the melt flow. Presented at the January 1 (2018). https://doi.org/10.1117/12.2295798

Publisher's Note Springer Nature remains neutral with regard to jurisdictional claims in published maps and institutional affiliations.

Authors and Affiliations

Felix Zaiß[1] · John Powell[1] · Michael Haas[1,6] · Christian Diegel[2] · Klaus Schricker[2,7] · Jean Pierre Bergmann[2] · Christoph Spurk[3] · Marc Hummel[3,4] · Alexander Olowinsky[4] · Felix Beckmann[5] · Julian Moosmann[5] · Christian Hagenlocher[1] · Thomas Graf[1]

✉ Felix Zaiß
felix.zaiss@ifsw.uni-stuttgart.de

[1] University of Stuttgart, Institut für Strahlwerkzeuge (IFSW), Stuttgart, Germany

[2] Production Technology Group, Technische Universität Ilmenau, Gustav-Kirchhoff-Platz 2, 98693 Ilmenau, Germany

[3] Chair for Laser Technology LLT, RWTH Aachen University, Steinbachstraße 15, 52074 Aachen, Germany

[4] Fraunhofer-Institute for Laser Technology ILT, Steinbachstraße 15, 52074 Aachen, Germany

[5] Institute of Materials Physics, Helmholtz-Zentrum Hereon, Max-Planck-Str. 1, 21502 Geesthacht, Germany

[6] Graduate School of Excellence advanced Manufacturing Engineering, University of Stuttgart, Nobelstr. 12, 70569 Stuttgart, Germany

[7] Chair of Joining and Welding Technology, Brandenburg University of Technology, Konrad-Wachsmann-Allee 13, 03046 Cottbus, Germany